Geophysical Research Letters

RESEARCH LETTER
10.1029/2025GL114816

Large-Eddy Simulation of Internal Boundary Layers and Near-Surface Wind Estimation During Hurricane Landfalls

Xiaomin Chen[1] and **Christopher M. Rozoff**[2]

[1]University of Alabama in Huntsville, Huntsville, AL, USA, [2]Research Applications Laboratory, National Center for Atmospheric Research, Boulder, CO, USA

Key Points:

- A novel large-eddy simulation framework was further improved to study the internal boundary layer (IBL) during hurricane landfalls
- Twin log layers coexist within a narrow coastal transition zone
- Radar wind retrievals in principle can capture the IBL wind profile while estimating 10-m winds using radiosonde data is highly uncertain

Supporting Information:

Supporting Information may be found in the online version of this article.

Correspondence to:

X. Chen,
xiaomin.chen@uah.edu

Citation:

Chen, X., & Rozoff, C. M. (2025). Large-eddy simulation of internal boundary layers and near-surface wind estimation during hurricane landfalls. *Geophysical Research Letters*, *52*, e2025GL114816. https://doi.org/10.1029/2025GL114816

Received 11 JAN 2025
Accepted 15 MAY 2025

Author Contributions:

Conceptualization: Xiaomin Chen
Formal analysis: Xiaomin Chen
Investigation: Christopher M. Rozoff
Methodology: Xiaomin Chen
Software: Xiaomin Chen
Visualization: Xiaomin Chen, Christopher M. Rozoff
Writing – original draft: Xiaomin Chen
Writing – review & editing: Christopher M. Rozoff

Abstract Accurate estimation of coastal near-surface winds during hurricane landfalls remains challenging, partly attributable to an insufficient understanding of the wind profiles within the internal boundary layer (IBL) induced by an abrupt surface roughness change. This study addresses this issue by performing three semi-idealized large-eddy simulations. Results indicate that a nascent log layer emerges within the IBL, and its depth gradually increases from ∼60 m near the coast to ∼400 m 12 km inland, where the boundary layer transition is nearly complete. This nascent log layer is superimposed by another log layer originating from the upstream marine boundary layer. While turbulence kinetic energy (TKE) is maximized near the surface over both water and land, peak TKE values over land are a factor of 2 greater due to the amplified near-surface vertical wind shear. The capability and uncertainty of coastal radars and radiosondes to detect IBL and estimate 10-m winds are discussed.

Plain Language Summary Hurricane landfalls are typically associated with severe wind-related compound hazards (infrastructure damage, blackout, subsequent heatwaves during power outages, etc.) in the coastal region. Knowing exactly how strong near-surface winds will be during hurricane landfalls is crucial for risk communication, effective preparation of coastal communities, and post-storm rescue and assistance (e.g., by FEMA). However, this intention is compromised by our limited understanding of the evolution of near-surface winds during landfalls, partly attributable to the scarcity of the coordinated observations of low-level winds over both water and land. Using specially configured turbulence-resolving computer model simulations, this study provides insights into the effects of land surface types and distance inland on the near-surface wind profile. This study also quantifies the uncertainty of the 10-m wind estimate derived from different observation-based approaches for *the first time*. These findings can guide future field campaigns and hurricane landfall studies.

1. Introduction

Hurricane landfalls are associated with hazardous winds threatening the lives and properties of communities in coastal regions and further inland. Accurately predicting and estimating near-surface winds during hurricane landfalls is crucial for evacuation, warnings, and post-hurricane assistance and recovery. Over the open ocean, the nearly neutral hurricane boundary layers (HBLs) are typically associated with logarithmic near-surface wind profiles (i.e., the log layer) below the jet (Franklin et al., 2003; Powell et al., 2003). The log-layer depth varies in high-wind conditions, varying from ∼150 m at major-hurricane-force winds to a few hundred meters at tropical-depression-force winds (Richter et al., 2021).

The robustness of this *single* near-surface log layer is challenged during hurricane landfalls when an abrupt increase of surface roughness length (z_0) significantly decelerates the near-surface winds, inducing the development of an internal boundary layer (IBL) over land (e.g., Hirth et al., 2012; Knupp et al., 2006). This factor potentially accounts for the inconsistency in earlier observational studies regarding the existence of a log layer over land (e.g., Krupar et al., 2016; Tsai et al., 2019). Tsai et al. (2019) observed a log layer with its depth varying between 60 and 240 m near the coast during the landfall of two super typhoons. In contrast, Krupar et al. (2016) reported that the log-law fit of the radar-retrieved wind profile below 300 m height or the jet level can induce a significant weak bias of the estimated 10-m winds in the analysis of 17 landfalling hurricanes, and thereby concluded that the log law is not an appropriate methodology to estimate the near-surface winds over land for landfalling hurricanes. Despite this uncertainty, the log-layer assumption is frequently adopted to estimate overland 10-m winds from radar-beam height winds (Alford et al., 2019, 2024; Kosiba & Wurman, 2014; Takahashi & Nolan, 2024).

Additionally, the Monin–Obukhov similarity theory is used in surface-layer parameterizations in numerical weather prediction (NWP) models (e.g., Chen et al., 2022; Olson et al., 2021), which dictates a logarithmic wind profile under neutral boundary layer conditions. Thus, the uncertainty of the log layer over land also impairs the accuracy of the model-predicted HBL wind profile (including 10-m winds). To improve the model guidance of near-surface winds over land, it is imperative to understand the evolution of near-surface wind profiles during hurricane landfalls. However, near-surface wind observations—that are spatially and temporally continuous from water to land—are typically unavailable. Motivated by these limitations, this study will leverage a novel large-eddy simulation (LES) framework to examine the IBL processes during hurricane landfalls over homogeneous land surface conditions. Specifically, questions to be addressed include:

1. How does the IBL evolve in the coastal region?
2. Does the log layer assumption still hold during the landfall of HBLs?
3. How to better estimate the overland 10-m winds using observations?

2. Methods

2.1. Modeling Framework

A recently developed small-patch LES modeling framework was used to study hurricane landfalls (cf. les-coast) (Rozoff et al., 2023; R23 hereafter). This framework, available in Cloud Model 1 (CM1; Bryan & Fritsch, 2002), is adopted in this study. As a descendant of a "simple" method for simulating HBLs (Bryan et al., 2017; Chen, Bryan, et al., 2021, C21 hereafter), the les-coast framework includes realistic large-scale dynamic forcing by specifying three parameters, that is, gradient wind speed V, its radial gradient of $\partial V/\partial r$, and the distance to the hurricane center R. This feature allows a small-patch LES domain with grid spacings of O(10 m), which is computationally much more efficient than the LES for entire TC circulations extending a few hundred kilometers with relatively coarser grid spacings. Built upon R23, this study includes a large-scale nudging toward the thermodynamic profiles derived from actual HBLs over the LES ocean subdomain, similar to C21. This special setup allows LESs to produce more realistic turbulent fluxes against in-situ aircraft measurements (C21). The detailed model setup is documented in Text S1 in Supporting Information S1. Three LES experiments are conducted with varying land-use/land-cover categories, that is, cropland/woodland mosaic, wooded wetland, and urban and built-up land. Their corresponding surface roughness length z_0 is 0.2, 0.4, and 0.8 m, respectively, ∼3 orders greater than the z_0 of water. Hereafter, these LES experiments are referred to as LES-z02, LES-z04, and LES-z08, respectively. These LESs are integrated forward for 3 hr. Similar to R23, a steady state (in terms of the domain-averaged surface winds and turbulent variables) quickly arrives after 30 min. The homogeneous land-use experiments here covering a significant range of z_0 values provide a range of uncertainty to help interpret more complex land use. HBLs exposed to more complex, heterogeneous land conditions will be the focus of future research.

2.2. Analysis Methods

The analysis period focuses on the steady state during $t = 2$–3 hr. Considering the horizontal inhomogeneity of z_0 in the east-west direction, results shown below are averaged along the y-axis, unless specified otherwise, and then temporally averaged using the 1-min output during $t = 2$–3 hr. Similar to C21, the turbulence kinetic energy (TKE) is defined as $0.5(\overline{u'u'} + \overline{v'v'} + \overline{w'w'}) + e_s$, where u, v, and w are three components of velocity, and overbars denote the average along the y-axis, prime denotes the perturbations from the y-axis average (e.g., $u' = u - \overline{u}$), and e_s is the subgrid TKE.

As an IBL develops over land due to the rapid change of z_0, the IBL height h_{IBL} under neutral or unstable conditions can be calculated as (Arya, 2001; Peterson, 1969; Powell et al., 1996):

$$h_{\mathrm{IBL}} = \alpha z_0 \left(\frac{X}{z_0}\right)^{0.8}, \tag{1}$$

where α is an empirical constant dependent on stability with values between 0.2 and 0.8 (Stull, 1988), z_0 represents the land surface roughness, and X is the distance downwind of the surface roughness change (i.e., the coast). Our results indicate that using Equation 1 and $\alpha = 0.28$ effectively predicts the IBL height over land in

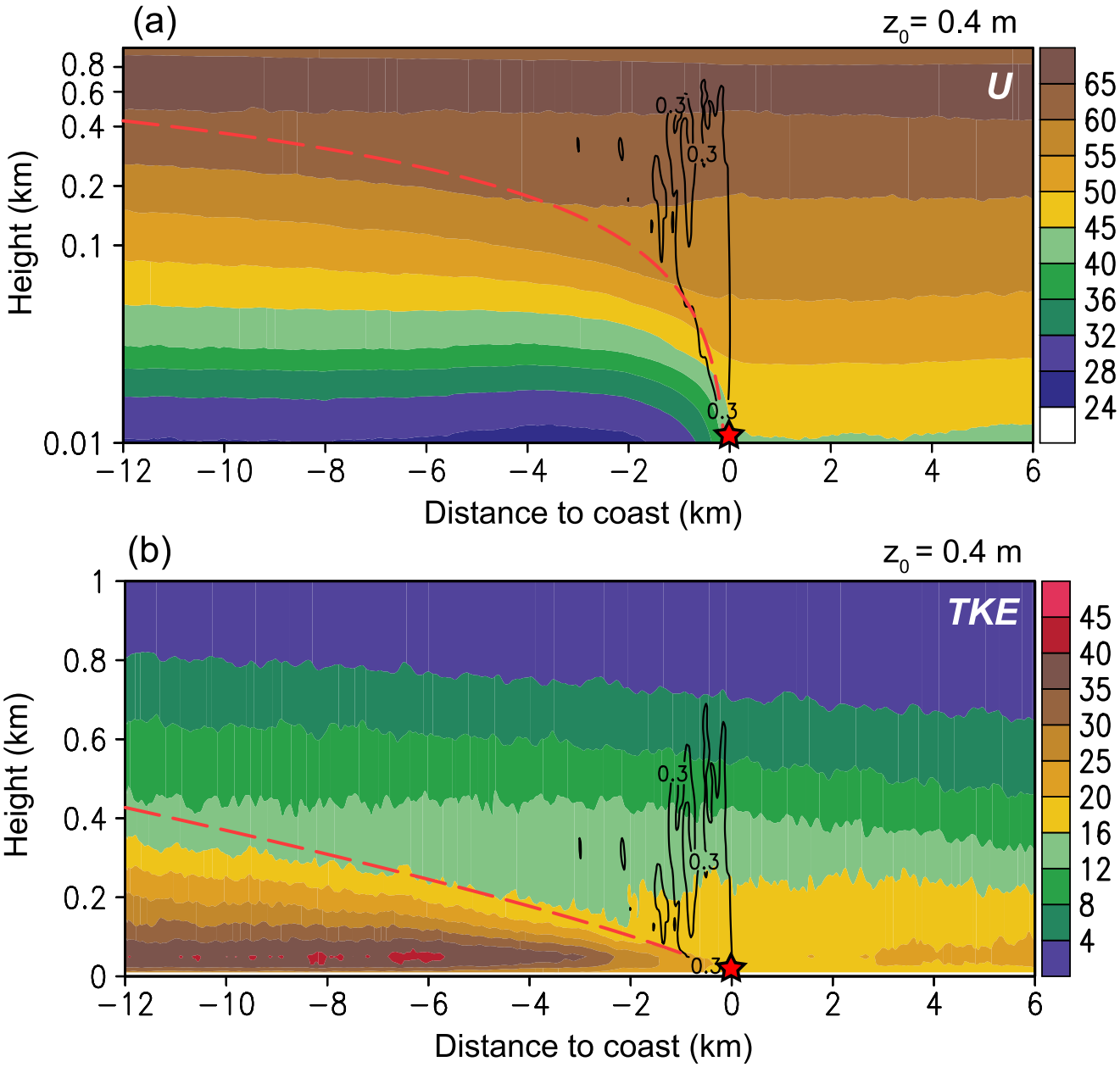

Figure 1. (a, b) The composite structure of horizontal wind speeds (m s^{-1}, shading) and TKE (m^{-2} s^{-2}, shading), respectively, over t = 2–3 hr for LES-z04. Black contours denote the composite vertical velocity (i.e., w = 0.3 m s^{-1}), and the red star marks the landfall location (x = 0 km). Distance inland corresponds to negative x values. The red dashed line denotes the IBL height using Equation 1 with α = 0.28.

three LESs (see Figure 1 and Figure S2 in Supporting Information S1), consistent with earlier studies (Wood, 1982).

3. Results

3.1. The IBL Development and Near-Surface Log Layer Over Land

Figure 1a presents the composite vertical structure of wind speeds averaged along the y-axis during t = 2–3 hr for the LES-z04 experiment. The log-scale height coordinate is used to enhance the visualization of the wind structure within the shallow IBL. During the ocean-to-land transition of HBL, winds near the jet level are nearly unaffected, consistent with an earlier modeling study Tuleya (1994) and radar observations (Hirth et al., 2012). In contrast, the

low-level onshore flow, especially in the lowest 100 m, is prominently decelerated due to the rapid increase of surface friction, forming an IBL. For reference, the diagnosed h_{IBL} using Equation 1 is provided in Figure 1a (see the red dashed line), which closely follows the region of decelerated wind speeds. The deceleration of onshore flow induces low-level convergence along the coast that produces organized updrafts (>0.3 m s^{-1}) against the stable stratification in terms of θ. Interestingly, the minimum near-surface winds over land occur within $x = -2$ to -6 km; further inland, the magnitude of near-surface winds slightly bounces up as the IBL deepens, likely attributable to the turbulence mixing of high momentum aloft downward. A similar phenomenon is also found in the other two experiments (e.g., Figure S2b in Supporting Information S1).

To further examine the evolution of the IBL over land, Figure 1b shows the composite vertical structure of TKE averaged over the same period. Over both ocean and land, the TKE is maximized near the surface and decreases with height. The peak value of TKE over land is >40 m^2 s^{-2}, approximately a factor of 2 greater than that over the ocean, indicating stronger shear production of TKE over land. The abrupt increase of TKE from ocean to land indicates a rapid development of the IBL overland, which leads to enhanced vertical gradient of TKE at the lower levels where TKE is >16 m^2 s^{-2}. Regions with TKE > 16 m^2 s^{-2} extend upward further inland, confirming that the vertical growth of IBL is a function of the distance inland (i.e., X). Interestingly, the h_{IBL} using Equation 1 nearly follows the region of high TKE values (i.e., >16 m^2 s^{-2}). The h_{IBL} increases from 60 m at $x = -1$ km to ~400 m at $x = -12$ km. Similarly, h_{IBL} well predicts the growth of IBL in the other two LES experiments (see Figures S2c and S2d in Supporting Information S1). Comparison of the h_{IBL} in the three LESs (Figure 1b and Figures S2c and S2d in Supporting Information S1) indicates greater h_{IBL} for larger z_0 values at the same x (e.g., $x = -12$ km); this behavior is predicted by Equation 1 as h_{IBL} is proportional to z_0. Above the IBL, the TKE structure retains the pattern of the upstream marine HBL, particularly above 400 m, but it is vertically displaced upward during the transition from water to land, likely attributable to the vertical advection of TKE related to the organized updrafts along the coast. Interestingly, high TKE values of >16 m^2 s^{-2} from the marine HBL extend to 2 km inland, where the updraft dominates. As the upward TKE advection weakens further inland, TKE weakens in the 200–300 m layer within a short distance until the IBL becomes dominant.

To examine the evolution of wind profiles from water to land, Figure 2 shows the wind profiles extracted at $x = -1, -3, -6$, and -12 km from the composite wind structure in Figure 1a. For reference, the marine HBL wind profile at $x = 1$ km is provided (see the black line), indicating a ~500-m deep, quasi-log layer below the jet over ocean. Most of the 10-m wind deceleration occurs within just 1 km inland, where wind speed decreases logarithmically with height below ~50 m (i.e., within the nascent IBL, see Figure 1b). This near-surface log layer subsequently grows upward with the distance inland and reaches ~400 m at $x = -11$ km, suggesting the HBL transition from ocean to land is nearly complete. The ~12 km length scale of the HBL transition zone during hurricane landfalls is aligned with earlier radar observations (Alford et al., 2020; Knupp et al., 2006). Comparison of Figure 2 and Figure S3 in Supporting Information S1 indicates that the 1-km rapid deceleration zone and the fast growth of the near-surface log layer with the distance inland remain robust for all three experiments. At the same x, higher z_0 corresponds to the more prominent deceleration of the 10-m wind and slightly deeper near-surface log layer (Figure S4 in Supporting Information S1).

Importantly, the nascent log layer coexists with the original log layer from the upstream marine HBL until the completion of the HBL transition, when the wind profile is fully adjusted to the new z_0 over land and the depth of the new log layer is comparable to that over the ocean.

3.2. Subdomain-Averaged Wind Profiles and Their Implication on Doppler Radar Wind Retrievals

One popular approach to obtaining the coastal HBL wind profile is applying the Velocity Azimuth Display (VAD) technique (Browning & Wexler, 1968) to the ground-based Doppler velocity data. Since each volume scan from typical operational radars takes ~6 min and the VAD retrieval domain is prescribed, the retrieved VAD winds represent a spatiotemporal average. Given this, Figure 2 presents the wind profile averaged within the land subdomain over $t = 2$–3 hr (gray dotted line). While the spatial and temporal averaging in the LES differ from that in the VAD analysis of actual radar data, this LES-derived mean wind profile can provide insights into the HBL features observed by radars within the coastal transition zone. Notably, the LES-based mean wind profile captures the twin log layers representative of an average between $x = -6$ and -11 km, suggesting that the VAD analysis of the Doppler velocity data– with sufficient vertical resolutions (ideally ≤ 30 m, given the shallow nature of IBLs) can, in principle, resolve the log layer within the IBL. As the antenna height of coastal radars in the United States

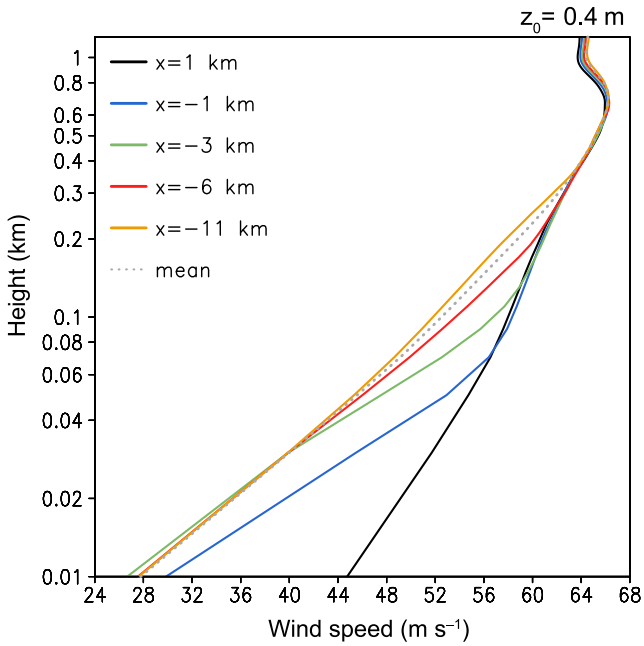

Figure 2. The composite wind profile at various distances inland (negative x values, colored lines) and 1 km upstream of the coastline (black). The gray dashed line denotes the average within the land subdomain (gray dashed). Results are averaged along the y-axis and over t = 2–3 hr for LES-z04.

is above 25 m (not shown), one can retrieve the 10-m winds using the VAD wind profile within the IBL, whose depth varies from tens to a few hundred meters (see Figure 2).

3.3. Sampling of Virtual Sondes Released in the Coastal Area

GPS sondes are effective instrument platforms for obtaining near-surface wind profiles in HBLs. Winds are derived from the change of the sonde's GPS locations, with additional adjustment by applying low-pass filters (Giammanco et al., 2013; Hock & Franklin, 1999). The latest dropsonde records wind at 2–4 Hz (Aberson et al., 2023) while radiosondes typically record winds every 1-to-5 seconds, suggesting gust features may be sampled. However, the composite wind profiles from sondes represent an ensemble mean smoothing out the gusty or convective features. Thus, sondes provide an effective approach to derive representative HBL wind profiles. The dropsonde composite of wind profiles in the HBL over ocean indicates the existence of a near-surface log layer at various surface wind speeds (Franklin et al., 2003; Powell et al., 2003; Richter et al., 2021). As dropsondes are rarely released in the coastal region due to safety protocols, radiosondes are used to sample the coastal HBL wind profiles. Depending on the distance of the release site from the coast, radiosondes may sample both the IBL and the original marine HBL at various distances inland during their ascent. The representation of the single or composite radiosonde wind profiles becomes unclear, demanding careful investigations.

Inspired by the composite wind profiles discussed in section 3a, 101 virtual radiosondes, spaced every 20 m within y = 0.5–2.5 km, are released at $x = -1$, -3, -6, and -9 km, respectively. The release height is 10 m (i.e., the bottom half model level), and the balloon rising speed (w_b) is set to 5 m s^{-1} based on the NWS documentation (https://www.weather.gov/upperair/factsheet). These virtual sondes are initialized at t = 2 hr and tracked forward for 200 s or shorter before they leave the horizontal domain or ascend above 1-km height. The LESs are restarted at t = 2 hr with 1-s output for trajectory analyses. The trajectory is calculated using the predictor-corrector technique (Chen, Gu, et al., 2021; Onderlinde & Nolan, 2016). This technique uses the winds at the predicted midpoint plus w_b to advect the sonde at the initial location for a full-time step. The predicted midpoint is determined by advecting the sonde from the initial location by a half-time step using the wind information plus w_b at the initial location. The time step is set to 1 s, consistent with the output frequency of the LES restart run. To mimic the GPS sondes' wind calculation, midpoint wind information and height are recorded by virtual sondes.

To illustrate the turbulent features sampled by virtual sondes in the HBL, Figure 3a shows the 10-m wind speed at t = 2 hr overlaid with trajectories of two virtual sondes released at $x = -6$ and $x = -1$ km, respectively, in LES-z04. Figure 3b further provides a lateral view of these trajectories. The fine-scale streaks are evident over land, supporting the notion that turbulence in the HBL is predominantly shear-driven (e.g., Foster, 2005; C21; R23). The two sondes are released at the locations of the maximum (red line) and minimum (blue line) 10-m winds among the 101 sondes at each x location. These sondes all sample the winds up to 500 m or higher before leaving the LES domain. Evidently, the sonde wind profile is a composite of different portions of downstream HBL wind structures at various levels and distances inland. This composite varies significantly even if the sondes are released at the same distance inland, as the sonde released at the minimum wind samples the near-surface wind profile more closely to the release site than that released at the location of the peak wind. For example, wind profiles of these two sondes starting from $x = -1$ km can be identified as the leftmost and rightmost profiles in Figure 4c, which indicate strikingly different low-level wind profiles and vertical wind shear (VWS).

Figures 4a–4c present the 101 wind profiles derived from virtual sondes released at $x = -6$, -3, and -1 km, respectively. The composite mean of these profiles (red line) indicates a shallow near-surface log layer below 60 m, and the slope of the red line is greater at $x = -6$ km than $x = -3$ and -1 km. The latter is consistent with the deepening of the IBL and reduced VWS further inland (cf. Figure 2). Similar to the approach adopted in earlier observational studies (e.g., Alford et al., 2019), the log-law fit of the lowest 500-m sonde winds (yellow line) was

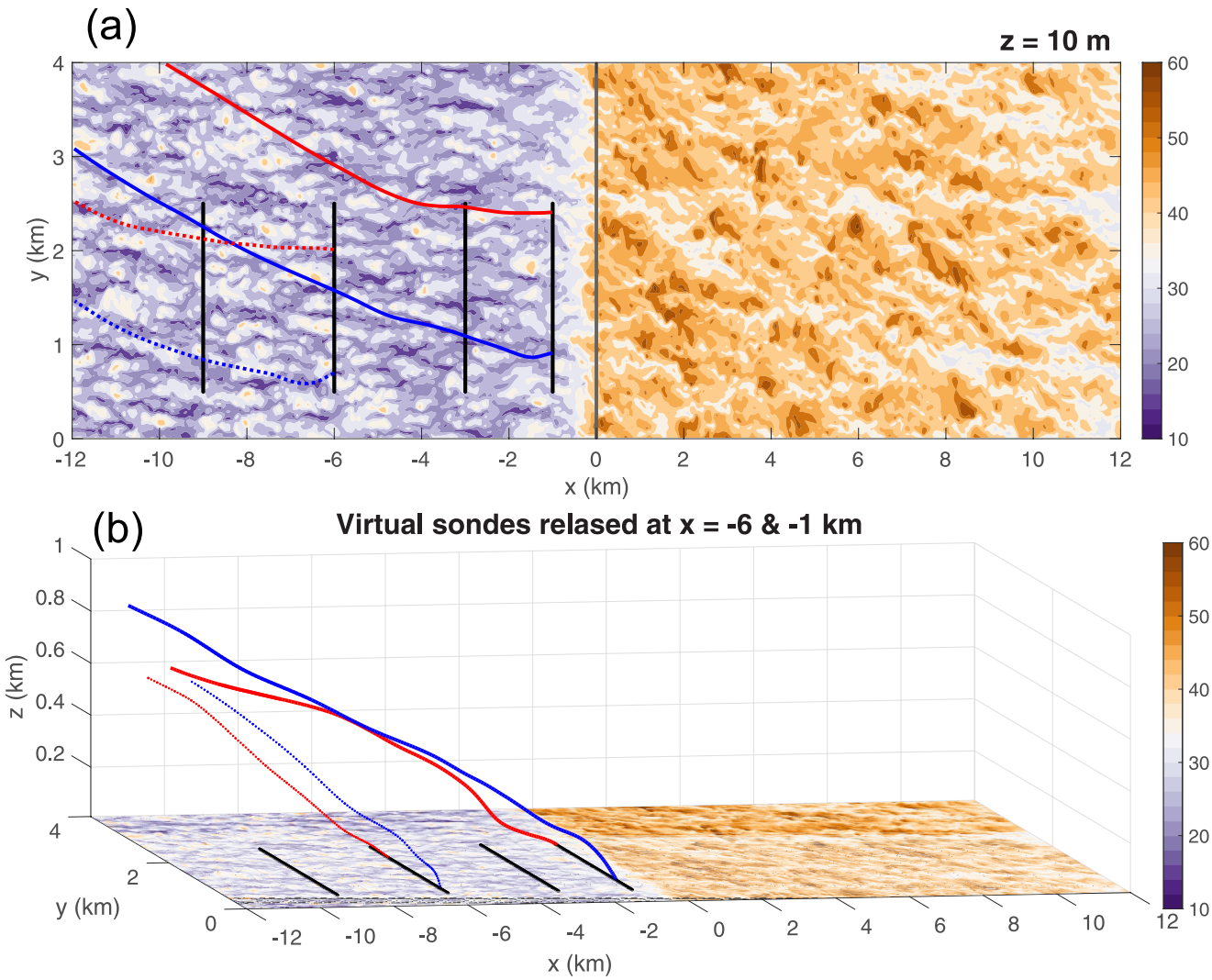

Figure 3. (a) 10-m wind speed (shading, m s^{-1}) at $t = 2$ hr for LES-z04. Black lines denote the virtual sonde release sites every 20 m within $y = 500$–2,500 m. The gray line marks the coastline. The solid red (blue) line is the plan view of the sonde trajectory released at the maximum (minimum) wind location at $x = -1$ km and $z = 0.01$ km. Similarly, dashed lines are for those released at $x = -6$ km. (b) A lateral view of these trajectories starting from $z = 0.01$ km. These trajectories last 200 s or shorter before they reach the lateral boundaries of the LES domain or above 1 km height.

performed to estimate the 10-m wind speed U_{10}. Results indicate a weak bias of the diagnosed U_{10} compared to the 1-min sustained winds (red circle) at $x = -3$ km and -6 km, and the weak bias increases with $|x|$, reaching -7 m s^{-1} at $x = -6$ km. Of note, the 1-min sustained winds at 10-m height are selected to match the definition of hurricane intensity by the National Hurricane Center. Choosing a longer averaging period (e.g., 2-min) produces similar results. Meanwhile, the estimated z_0 from the log-law fit indicates a high bias (compared to the truth $z_0 = 0.4$ m) that also increases with $|x|$ (see the legend on Figures 4a–4c).

Since releasing more than 100 sondes at the same x during hurricane landfalls is unfeasible, we applied the log-law fit for the wind profiles of 4 sondes randomly selected 1,000 times from the 101 sondes at each x location. This method generates the distribution of the estimated U_{10} bias and z_0 in box-and-whisker diagrams shown in Figures 4d–4i. To examine the sensitivity of the bias distribution to variations in log-law fit depth, three log-law fit depths including 200, 300, and 500 m are considered. As sondes released at $x = -9$ km do not have sufficient time to rise above 500 m, only the results corresponding to 200 and 300 m fit depths are shown. For comparison, we also test another method (e.g., Alford et al., 2024; Kosiba & Wurman, 2014) that combines the log-law

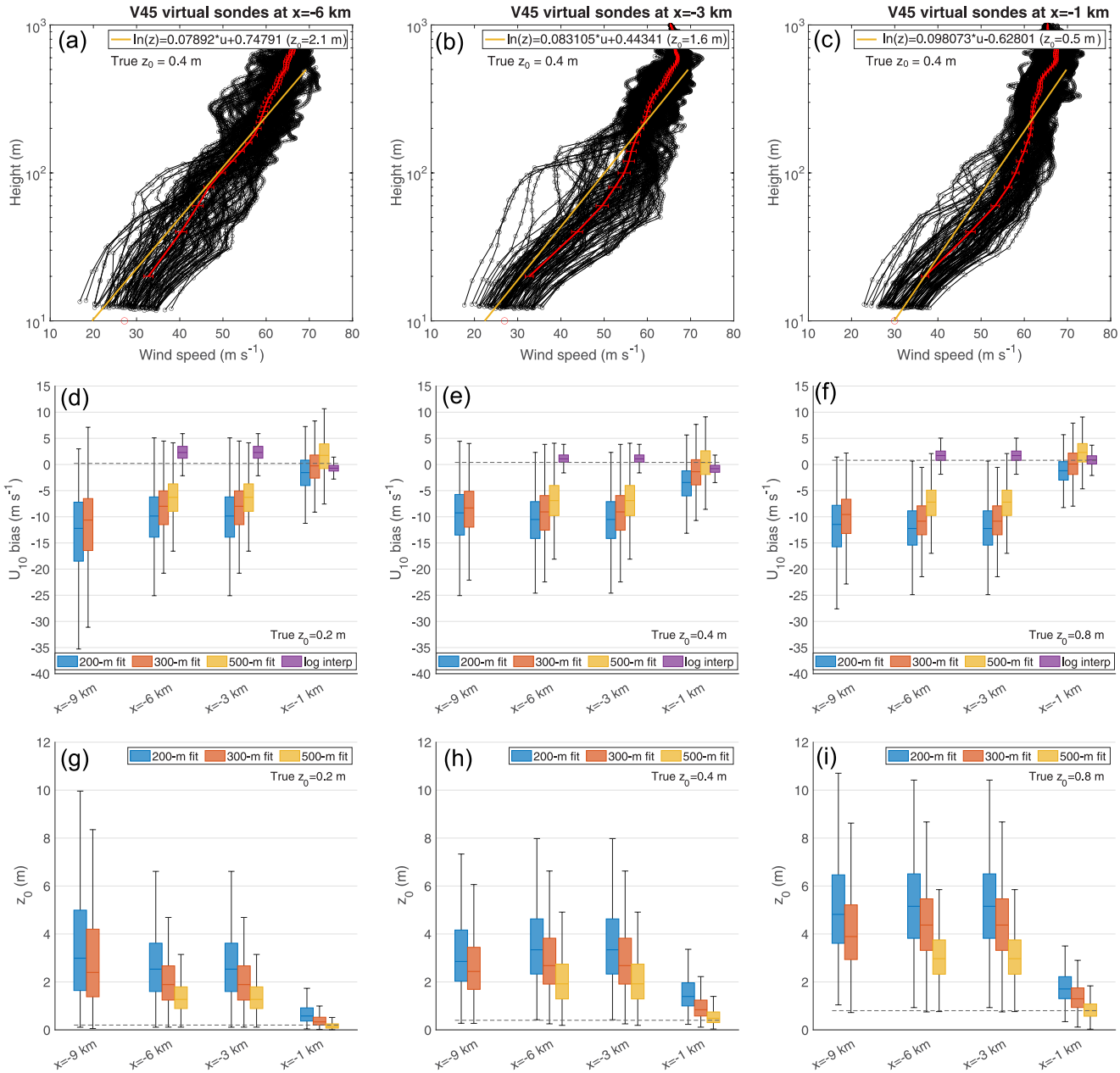

Figure 4. (a–c) The sampled wind profile from 100 virtual sondes released at $x = -9$ km, -6 km, and -3 km, respectively. Red circles at $z = 10$ m denote the 1-min wind speed averaged along the y-axis. The composite mean with standard error is shown as the red line with whiskers. The log-law fit for the winds below 500 m is shown as the orange line. (d–f) Box-and-whisker diagrams of the distribution of the U_{10} bias by randomly choosing 4 out of the 100 sondes 1,000 times at $x = -9$, -6, -3, and -1 km for three different land surfaces. The box-and-whisker diagram includes the 5th, 25th, 50th, 75th, and 95th percentiles with the interquartile range (IQR) shaded. (g–i) Similar to (d–f), but for the distribution of the retrieved z_0 from the log-law fit. True z_0 is provided as a gray dashed line on each panel.

equation, 500-m mean winds, and the actual z_0 to derive U_{10} (termed as *log-interp* hereafter, see purple bars in Figures 4d–4f):

$$U_{10} = U_{500}\frac{\ln 10 - \ln z_0}{\ln 500 - \ln z_0}. \quad (2)$$

Figures 4d–4i indicate that the increase of log-law fit depth from 200 to 500 m reduces the median and spread of U_{10} and z_0 bias. The minimum values of median U_{10} and z_0 bias related to the log-law fit occur at $x = -1$ km for all

LES experiments; further downstream, the median U_{10} weak bias can be as large as -12 m s^{-1}. Beyond 1 km inland, the chance of the log-law fit accurately predicting the true z_0 is rare, and the median value of the diagnosed z_0 for the 500-m log-law fit is approximately a factor of 4–5 greater than the actual z_0. Of note, a similar high bias of diagnosed z_0 from the log-law fit was reported by Alford et al. (2019) and alluded to by Giammanco et al. (2013).

In contrast to the large spread of U_{10} bias related to the log-law fit, the diagnosed U_{10} from *log-interp* indicates a much smaller bias with a more confined IQR. The peak U_{10} error is generally <5 m s^{-1} within 6 km inland for all LES experiments except for LES-z02 (Figure 4d). The median U_{10} bias is merely 1–2 m s^{-1} at $x = -6$ and -3 km and slightly negative at $x = -1$ km in LES-z02 and LES-z04 (Figures 4d and 4e). The encouraging performance of the *log-interp* approach can be explained by the nearly unaffected 500-m winds within 12 km land and the small difference in 10-m winds (~3 m s^{-1}) between the almost fully adjusted wind profile at $x = -11$ km and the initially perturbed wind profile at $x = -1$ km (cf. Figure 2).

4. Conclusions and Discussion

During hurricane landfalls, the abrupt increase of z_0 from water to land induces the formation of an IBL over land. Turbulence properties and wind profiles within the IBL are not well understood, which poses challenges in accurately estimating near-surface winds in the coastal region. Motivated by this issue, this study investigates the evolution of IBL during hurricane landfalls using a small-patch LES modeling framework (R23) with the additional inclusion of moisture and a nudging term toward the thermodynamic profiles over the ocean subdomain. This nudging term helps the LES produce more realistic vertical profiles of turbulence variables in marine HBL (C21). To examine the impact of z_0 on the IBL development, three LES experiments are conducted with $z_0 = 0.2$, 0.4, and 0.8 m, respectively. Effective approaches to estimate 10-m winds using coastal radar and radiosonde observations are discussed. Key findings are summarized below:

1. An IBL quickly develops onshore, whose depth is proportional to the distance inland and land z_0. While TKE values are maximized near the surface over both water and land, peak TKE values over land are approximately a factor of 2 greater due to the enhanced low-level vertical wind shear. The HBL transition is almost complete within 12 km inland, as the IBL depth becomes comparable to the marine log layer below the jet.
2. Twin log layers coexist within the coastal transition zone. One is the nascent near-surface log layer within the IBL, and the other originates from the upstream marine HBL. The depth of the IBL log layer increases with the distance inland as the IBL deepens.
3. With sufficient vertical resolution (ideally < 30 m), VAD analyses of Doppler radar observations can, in principle, capture the IBL wind profile and infer U_{10} using the log law.
4. The radiosonde wind profile is a composite of turbulent winds at various distances inland and heights. Estimating U_{10} using the log-law fit of a few sonde wind profiles is associated with a large spread of U_{10} bias. An increase of the log-law fit depth from 200 to 500 m significantly reduces the weak bias of U_{10} and high bias of z_0 in terms of the median values, and the smallest median bias occurs near the coast. In contrast, estimating U_{10} using *log-interp* induces smaller U_{10} errors generally within 5 m s^{-1}.

One caveat is these results do not claim the superiority of the *log_interp* approach over the log-law fit of the sonde winds, as they are drawn from a special set of LESs where the jet level remains unaffected at ~700 m during landfall. For a marine HBL with a jet below 500 m–such as in the eyewall of mature hurricanes (Alford et al., 2020)–the jet may be smoothed out by the vertical growth of the IBL, potentially diminishing the effectiveness of the log_interp approach (e.g., Takahashi & Nolan, 2024). Additionally, the spatial heterogeneity of actual land surfaces can potentially induce nested IBLs with multiple associated log layers in the HBL, further increasing the uncertainty in U_{10} estimation. Therefore, the magnitude of errors in 4) should be interpreted with caution when applied to real hurricane landfalls. Moreover, the idealized LES framework excludes convective downdrafts, whose impact on IBLs, log layers, and U_{10} estimates needs to be carefully assessed with the future development of this modeling framework.

Data Availability Statement

The source code of the CM1 model is available at https://www2.mmm.ucar.edu/people/bryan/cm1/downloadcode.html. The data related to each plot can be found at X. Chen and Rozoff (2025).

Acknowledgments
We gratefully acknowledge NOAA RDHPCS computer staff for maintaining the supercomputers used to perform these runs. We also thank Sim Aberson, Preston Pangle, and Kevin Knupp for generously sharing their expertise in wind measurements using sondes. Appreciation is extended to Geroge Bryan and two anonymous reviewers for their insightful comments that improved the quality of the analysis. This work was supported by the NSF Grant RISE-2438825. Lead author Xiaomin Chen was also supported by NOAA Grant NA23OAR4590380.

References

Aberson, S. D., Zhang, J. A., Zawislak, J., Sellwood, K., Rogers, R., & Cione, J. J. (2023). The NCAR GPS dropwindsonde and its impact on hurricane operations and research. *Bulletin of the American Meteorological Society*, *104*(11), E2134–E2154. https://doi.org/10.1175/BAMS-D-22-0119.1

Alford, A. A., Biggerstaff, M. I., Carrie, G. D., Schroeder, J. L., Hirth, B. D., & Waugh, S. M. (2019). Near-surface maximum winds during the landfall of Hurricane Harvey. *Geophysical Research Letters*, *46*(2), 973–982. https://doi.org/10.1029/2018GL080013

Alford, A. A., Schenkel, B., Hernandez, S., Zhang, J. A., Biggerstaff, M. I., Blumenauer, E., et al. (2024). Examining outer band supercell environments in landfalling tropical cyclones using ground-based radar analyses. *Monthly Weather Review*, *152*(10), 2265–2285. https://doi.org/10.1175/MWR-D-23-0287.1

Alford, A. A., Zhang, J. A., Biggerstaff, M. I., Dodge, P., Marks, F. D., & Bodine, D. J. (2020). Transition of the hurricane boundary layer during the landfall of Hurricane Irene (2011). *Journal of the Atmospheric Sciences*, *77*(10), 3509–3531. https://doi.org/10.1175/JAS-D-19-0290.1

Arya, S. P. (2001). *Introduction to micrometeorology* (2nd ed., p. 326). Academic Press.

Browning, K. A., & Wexler, R. (1968). The determination of kinematic properties of a wind field using Doppler radar. *Journal of Applied Meteorology and Climatology*, *7*(1), 105–113. https://doi.org/10.1175/1520-0450(1968)007<0105:TDOKPO>2.0.CO;2

Bryan, G. H., & Fritsch, J. M. (2002). A Benchmark simulation for moist nonhydrostatic numerical models. *Monthly Weather Review*, *130*(12), 2917–2928. https://doi.org/10.1175/1520-0493(2002)130<2917:ABSFMN>2.0.CO;2

Bryan, G. H., Worsnop, R. P., Lundquist, J. K., & Zhang, J. A. (2017). A simple method for simulating wind profiles in the boundary layer of tropical cyclones. *Boundary-Layer Meteorology*, *162*(3), 475–502. https://doi.org/10.1007/s10546-016-0207-0

Chen, X., Bryan, G. H., Hazelton, A., Marks, F. D., & Fitzpatrick, P. (2022). Evaluation and improvement of a TKE-based eddy-diffusivity mass-flux (EDMF) planetary boundary layer scheme in hurricane conditions. *Weather and Forecasting*, *37*(6), 935–951. https://doi.org/10.1175/WAF-D-21-0168.1

Chen, X., Bryan, G. H., Zhang, J. A., Cione, J. J., & Marks, F. D. (2021). A framework for simulating the tropical-cyclone boundary layer using large-eddy simulation and its use in evaluating PBL parameterizations. *Journal of the Atmospheric Sciences*, *78*(11), 3593–3611. https://doi.org/10.1175/JAS-D-20-0227.1

Chen, X., Gu, J.-F., Zhang, J. A., Marks, F. D., Rogers, R. F., & Cione, J. J. (2021). Boundary layer recovery and precipitation symmetrization preceding rapid intensification of tropical cyclones under shear. *Journal of the Atmospheric Sciences*, *78*(5), 1523–1544. https://doi.org/10.1175/JAS-D-20-0252.1

Chen, X., & Rozoff, C. M. (2025). DATA for "large-eddy simulation of internal boundary layers and near-surface wind estimation during hurricane landfalls". *Geophysical Research Letters. Zenodo*. https://doi.org/10.5281/zenodo.15216699

Foster, R. C. (2005). Why rolls are prevalent in the hurricane boundary layer. *Journal of the Atmospheric Sciences*, *62*(8), 2647–2661. https://doi.org/10.1175/JAS3475.1

Franklin, J. L., Black, M. L., & Valde, K. (2003). GPS dropwindsonde wind profiles in hurricanes and their operational implications. *Weather and Forecasting*, *18*(1), 32–44. https://doi.org/10.1175/1520-0434(2003)018<0032:GDWPIH>2.0.CO;2

Giammanco, I. M., Schroeder, J. L., & Powell, M. D. (2013). GPS dropwindsonde and WSR-88D observations of tropical cyclone vertical wind profiles and their characteristics. *Weather and Forecasting*, *28*(1), 77–99. https://doi.org/10.1175/WAF-D-11-00155.1

Hirth, B. D., Schroeder, J. L., Weiss, C. C., Smith, D. A., & Biggerstaff, M. I. (2012). Research radar analyses of the internal boundary layer over Cape Canaveral, Florida, during the landfall of Hurricane Frances (2004). *Weather and Forecasting*, *27*(6), 1349–1372. https://doi.org/10.1175/WAF-D-12-00014.1

Hock, T. F., & Franklin, J. L. (1999). The NCAR GPS dropwindsonde. *Bulletin of the American Meteorological Society*, *80*(3), 407–420. https://doi.org/10.1175/1520-0477(1999)080<0407:TNGD>2.0.CO;2

Knupp, K. R., Walters, J., & Biggerstaff, M. (2006). Doppler profiler and radar observations of boundary layer variability during the landfall of Tropical Storm Gabrielle. *Journal of the Atmospheric Sciences*, *63*(1), 234–251. https://doi.org/10.1175/JAS3608.1

Kosiba, K. A., & Wurman, J. (2014). Finescale dual-Doppler analysis of hurricane boundary layer structures in Hurricane Frances (2004) at landfall. *Monthly Weather Review*, *142*(5), 1874–1891. https://doi.org/10.1175/MWR-D-13-00178.1

Krupar, R. J., Schroeder, J. L., Smith, D. A., Kang, S.-L., & Lorsolo, S. (2016). A comparison of ASOS near-surface winds and WSR-88D-derived wind speed profiles measured in landfalling tropical cyclones. *Weather and Forecasting*, *31*(4), 1343–1361. https://doi.org/10.1175/WAF-D-15-0162.1

Olson, J. B., Smirnova, T., Kenyon, J. S., Turner, D. D., Brown, J. M., Zheng, W., & Green, B. W. (2021). *A description of the MYNN surface-layer scheme* (Vol. 67). NOAA Technical Memorandum OAR GSL. Retrieved from https://repository.library.noaa.gov/view/noaa/30605

Onderlinde, M. J., & Nolan, D. S. (2016). Tropical cyclone–relative environmental helicity and the pathways to intensification in shear. *Journal of the Atmospheric Sciences*, *73*(2), 869–890. https://doi.org/10.1175/JAS-D-15-0261.1

Peterson, E. W. (1969). Modification of mean flow and turbulent energy by a change in surface roughness under conditions of neutral stability. *Quarterly Journal of the Royal Meteorological Society*, *95*(405), 561–575. https://doi.org/10.1002/qj.49709540509

Powell, M. D., Houston, S. H., & Reinhold, T. A. (1996). Hurricane Andrew's landfall in south Florida. Part I: Standardizing measurements for documentation of surface wind fields. *Weather and Forecasting*, *11*(3), 304–328. https://doi.org/10.1175/1520-0434(1996)011<0304:HALISF>2.0.CO;2

Powell, M. D., Vickery, P. J., & Reinhold, T. A. (2003). Reduced drag coefficient for high wind speeds in tropical cyclones. *Nature*, *422*(6929), 279–283. https://doi.org/10.1038/nature01481

Richter, D. H., Wainwright, C., Stern, D. P., Bryan, G. H., & Chavas, D. (2021). Potential low bias in high-wind drag coefficient inferred from dropsonde data in hurricanes. *Journal of the Atmospheric Sciences*, *78*(7), 2339–2352. https://doi.org/10.1175/JAS-D-20-0390.1

Rozoff, C. M., Nolan, D. S., Bryan, G. H., Hendricks, E. A., & Knievel, J. C. (2023). Large-eddy simulations of the tropical cyclone boundary layer at landfall in an idealized urban environment. *Journal of Applied Meteorology and Climatology*, *62*(11), 1457–1478. https://doi.org/10.1175/JAMC-D-23-0024.1

Stull, R. B. (1988). *An introduction to boundary layer meteorology* (p. 596). Kluwer Academic Publishers.

Takahashi, T., & Nolan, D. S. (2024). The vortex structure and near-surface winds of Typhoon Faxai (2019) during landfall. Part I: Observational analysis. *Quarterly Journal of the Royal Meteorological Society*, *150*(759), 1172–1193. https://doi.org/10.1002/qj.4641

Tsai, Y.-S., Miau, J.-J., Yu, C.-M., & Chang, W.-T. (2019). Lidar observations of the typhoon boundary layer within the outer rainbands. *Boundary-Layer Meteorology*, *171*, 237–255. https://doi.org/10.1007/s10546-019-00427-6

Tuleya, R. E. (1994). Tropical storm development and decay: Sensitivity to surface boundary conditions. *Monthly Weather Review*, *122*(2), 291–304. https://doi.org/10.1175/1520-0493(1994)122<0291:TSDADS>2.0.CO;2

Wood, D. H. (1982). Internal boundary layer growth following a step change in surface roughness. *Boundary-Layer Meteorology*, *22*(2), 241–244. https://doi.org/10.1007/BF00118257

References From the Supporting Information

Bryan, G. H. (2022). Options for large-eddy simulations of hurricane boundary layers in CM1 (and other numerical models). In *35th Conference on Hurricanes and Tropical Meteorology* (Vol. 11C.4). American Meteorological Society. Retrieved from https://ams.confex.com/ams/35Hurricanes/meetingapp.cgi/Paper/402171

Chen, J., & Chavas, D. R. (2020). The transient responses of an axisymmetric tropical cyclone to instantaneous surface roughening and drying. *Journal of the Atmospheric Sciences*, *77*(8), 2807–2834. https://doi.org/10.1175/JAS-D-19-0320.1

Cione, J. J. (2015). The relative roles of the ocean and atmosphere as revealed by buoy air–sea observations in hurricanes. *Monthly Weather Review*, *143*(3), 904–913. https://doi.org/10.1175/MWR-D-13-00380.1

Cione, J. J., Black, P. G., & Houston, S. H. (2000). Surface observations in the hurricane environment. *Monthly Weather Review*, *128*(5), 1550–1561. https://doi.org/10.1175/1520-0493(2000)128<1550:SOITHE>2.0.CO;2

Deardorff, J. W. (1980). Stratocumulus-capped mixed layers derived from a three-dimensional model. *Boundary-Layer Meteorology*, *18*(4), 495–527. https://doi.org/10.1007/BF00119502

Hlywiak, J., & Nolan, D. S. (2021). The response of the near-surface tropical cyclone wind field to inland surface roughness length and soil moisture content during and after landfall. *Journal of the Atmospheric Sciences*, *78*(3), 983–1000. https://doi.org/10.1175/JAS-D-20-0211.1

Powell, M. D. (1987). Changes in the low-level kinematic and thermodynamic structure of Hurricane Alicia (1983) at landfall. *Monthly Weather Review*, *115*(1), 75–99. https://doi.org/10.1175/1520-0493(1987)115<0075:CITLLK>2.0.CO;2